Quantitative Optical Coherence Elastography: A Novel Intensity-Based Inversion Method Versus Strain-Based Reconstructions

Lisa Krainz, *Graduate Student Member, IEEE*, Ekaterina Sherina, Simon Hubmer, Mengyang Liu, Wolfgang Drexler, and Otmar Scherzer

***Abstract*—Many diseases like cancer or atherosclerosis bear micro-scale tissue stiffness changes, which can be visualised by optical coherence elastography (OCE). OCE is a promising research field, where a growing number of publications present qualitative displacement maps. Quantitative OCE results have also been presented, but still lack high precision and good reproducibility, which are important for clinical applications. In this work, we compare three reconstruction methods for the Young's modulus in intensity-based quasi-static compressional OCE: uniaxial analysis, strain map based reconstruction facilitating a particle tracking improved optical flow (EOFM), and a novel image-based inverse reconstruction method (IIM). The quality of the proposed reconstruction methods is investigated by comparing their performance on twelve silicone elastomer phantoms with inclusions of varying size and stiffness. While the uniaxial reconstruction is strongly affected by lateral motion, EOFM is capable of deriving precise strain maps from consecutive OCT images during compression. However, for a valid Young's modulus reconstruction additional stress map information is required. IIM performs best, precisely reconstructing Young's modulus of inclusion and background, closely corresponding to separately determined ground truth values. The method offers a significant improvement of the relative error by a factor of 3.5 compared to uniaxial and strain-based analysis.**

Manuscript received 4 July 2022; revised 3 November 2022; accepted 23 November 2022. Date of publication 28 November 2022; date of current version 14 December 2022. This work was supported by the Austrian Science Fund (FWF) under Projects F6803-N36, F6805-N36, and F6807-N36 through the Special Research Programme SFB F68: "Tomography Across the Scales". The work of Otmar Scherzer was supported by the National Foundation for Research, Technology and Development, Austrian Federal Ministry for Digital and Economic Affairs and in part by Christian Doppler Research Association. The work of Mengyang Liu was supported by EU H2020 Marie Skłodowska-Curie Actions Project "SkinOptima" under Grant 894325. *(Lisa Krainz and Ekaterina Sherina are co-first authors.) (Corresponding author: Lisa Krainz.)*

Lisa Krainz and Wolfgang Drexler are with the Center for Medical Physics and Biomedical Engineering, Medical University of Vienna, 1090 Vienna, Austria (e-mail: lisa.krainz@meduniwien.ac.at; wolfgang.drexler@meduniwien.ac.at).

Ekaterina Sherina is with the Faculty of Mathematics, University of Vienna, 1090 Vienna, Austria (e-mail: ekaterina.sherina@univie.ac.at).

Simon Hubmer is with the Johann Radon Institute Linz, 4040 Linz, Austria (e-mail: simon.hubmer@ricam.oeaw.ac.at).

Mengyang Liu is with the Center for Medical Physics and Biomedical Engineering, Medical University of Vienna, 1090 Vienna, Austria, and also with the Singapore Eye Research Institute and the Singapore National Eye Centre, Singapore (e-mail: mengyang@udel.edu).

Otmar Scherzer is with the Faculty of Mathematics, University of Vienna, 1090 Vienna, Austria, and also with the Christian Doppler Laboratory for Mathematical Modeling and Simulation of Next Generations of Ultrasound Devices (MaMSi), 1090 Vienna, Austria (e-mail: otmar.scherzer@univie.ac.at).

Color versions of one or more figures in this article are available at https://doi.org/10.1109/JSTQE.2022.3225108.

Digital Object Identifier 10.1109/JSTQE.2022.3225108

***Index Terms*—Inverse Problems, Optical Coherence Elastography, Quantitative Reconstruction, Stiffness, Young's Modulus.**

I. Introduction

ELASTOGRAPHY pioneered in ultrasound imaging, where it is used to add mechanical contrast to the 3D imaging data, e.g., in cancer detection [1], [2], [3], [4], evaluation of benign lesions of the musculoskeletal system [5], or assessment of tendon injuries [6].

Meanwhile, the concept of elastography was adapted in the field of magnetic resonance imaging as well, where it is used to visualize the mechanical behavior of internal organs [7], [8], [9] and other human body parts, e.g. arterial walls [10] or breast tumors [11]. Both ultrasound imaging and magnetic resonance imaging work with resolutions in the millimeter range, but for some applications like early cancer detection [12], [13], investigating various eye diseases [14], [15] or detection of arterial rigidifications [16], micro-scale elastographic imaging is necessary.

While optical coherence tomography (OCT) was introduced in 1991 by Huang et al. [17] and the idea of using it for elastography was published already in 1998 by Schmitt under the name of optical coherence elastography (OCE) [18], it is gaining new popularity in recent years. Originally, Schmitt used a time domain OCT (TD-OCT) system and a piezoelectric actuator for compressing a gelatine phantom with enclosed latex spheres, pork meat, and an in-vivo human finger. He presented a cross-correlation as well as an optical flow method to estimate the resulting strain quantitatively, and observed that OCT imaging speed needs to be improved to obtain reasonable OCE results on in-vivo samples, due to blood circulation, heartbeat and motion artefacts. This is the reason why the next impactful OCE publication took eight more years, until after spectral domain OCT (SD-OCT) was initiated. SD-OCT significantly improved the OCT technology in terms of speed, phase sensitivity and resolution. Kirkpatrick et al. [19] presented two speckle tracking algorithms, one for small and the other for large deformations, and applied their method on a polyvinyl alcohol phantom using an SD-OCT system. Currently, OCE evolves in two directions: The biggest recent advances in OCE focus on non-contact OCE without external load, as demonstrated by Nair et al. [20], using

only a rabbit's heartbeat to perform OCE on its cornea. In parallel to these qualitative achievements, the quality improvement of quantitative OCE results is an ongoing goal.

Phase-sensitive OCE, convincing through its high axial resolution and easy analysis, is the most common choice for OCE [21]. For the benefit of phase stability between single loading steps, fast loading mechanisms are necessary and the acquisition of 3D volumes usually requires loading step repetition [22]. While the repeatability of any mechanical loading steps suffers from Mullin's effect [23], the fast loading mechanism leads the way to dynamic OCE. In dynamic OCE and wave-based OCE, the loading follows a well-defined driving frequency and the frequency of the resulting tissue displacement is analysed to quantify the sample stiffness [24], [25]. While dynamic OCE has its advantages in contact-free loading and easiness of stiffness derivation, compressional OCE offers faster imaging speed and has the potential to deal with a broader stiffness range [26]. All phase-sensitive OCE methods suffer from a lack of information on the lateral sample expansion. The lateral displacement is not only crucial for any inverse modelling [27], but also has an impact on simple A-scan-wise OCE analysis. A good example of the issues caused by sidewards motion during phase-sensitive OCE can be found in the work of Li et al. [28], who analysed in detail the effect of sample lubrication on the quantitative results obtained through phase-sensitive OCE. They state that even in lubricated cases, the true stiffness is underestimated, indicating that the lateral displacement needs to be taken into account for a valid stiffness analysis. First ideas on how this issue could be addressed were mentioned in [29], e.g., using Doppler OCT or multiple off-axis beams. But these approaches can never achieve a lateral resolution close to the axial one of phase-sensitive OCE, and can also only work under certain geometrical constrains.To show the impact of the lateral expansion of a sample on its mechanical evaluation, a comparable axial and lateral resolution is desirable, which leaves intensity-based OCE as the only option.

In [30], Kurokawa et al. presented a correlation based approach which is able to determine in-plane as well as out-of-plane sub-μm displacements. This method later was expanded by Wijesinghe et al. to 3D images in [29], where also first elastographic results were shown. While these first results look promising, the method is currently limited to small displacements, comparable to phase-sensitive OCE, and is quite sensitive to noise, making spatial averaging important.

A number of different methods for strain computation have previously been presented. An often used approach is speckle tracking [31], [32], [33], which has the disadvantage of working only for very small displacements. The maximum detectable displacement is defined by the speckle decorrelation [19]. Also, various algorithms based on rigid body motion applicable to intensity-based OCE data were presented. Maximization of the cross-correlation coefficient between the unloaded image and a moving window over the loaded image is a commonly used method [29], [34]. A similar approach is applied in digital image correlation [32] and digital volume correlation techniques [35]. These methods suffer from a much lower resolution of the displacement map compared to the OCT image, since the resulting

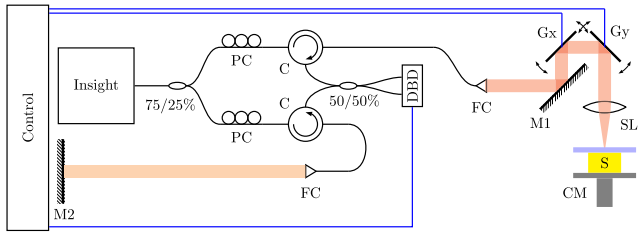

Fig. 1. OCE System: A non-commercial swept source OCT system is used and upgraded for elastography with a compression module. Insight: 1300 nm sweptsource, FC: fiber collimator, PC: polarization control, C: circulator, M1: tilted mirror, M2: mirror of the reference arm, Gx and Gy: galvanometers, SL: scan lens, S: sample, CM: compression module (symbolic picture), DBD: dual balance detector, Control: PC and galvo drivers.

resolution is governed by the kernel size used for the correlation. Another recently proposed method is optical flow (OF), designed for apparent motion detection from brightness patterns in an image [36], [37], [38]. Optical flow was first described by Horn and Schunck [39] in 1981 and is since used as a common tool for motion estimation and video processing in a variety of branches, e.g. in street traffic analysis [40] or in preclinical image analysis [41].

In this work, we reconstruct the Young's modulus from intensity-based OCE data using an inversion method, emphasising the impact of the lateral sample expansion. We benchmark these results against the results of a simple uniaxial reconstruction method and a strain-map based method with uniform stress assumption, applied to the same phantoms. For finding the respective strain-maps, we apply a novel particle tracking improved optical flow algorithm developed in [42], [43], which corrects the observed non-physicality of standard OF estimates from intensity-based OCE data. Twelve silicone elastomer phantoms, within a schema of varying inclusion and background stiffness as well as inclusion sizes, are used to investigate the capabilities of all three methods. Our analysis shows that the lateral sample expansion as well as stress non-uniformity are crucial aspects for a correct quantitative stiffness analysis. We further show that the inclusion size as well as the inclusion-background stiffness ratio have only a small influence on the quality of the quantitative analysis.

II. Methods

A. OCT System

The key technological component of our fiber-based OCT setup (see Fig. 1) is an akinetic, highly phase stable Insight swept source (SLE-101, Insight Photonic Solutions, CO, US) with a central wavelength of $1297\ \mathrm{nm}$ and a $3\,\mathrm{dB}$ bandwidth of $29.8\,\mathrm{nm}$, operated at a repetition rate of about $230\,\mathrm{kHz}$. The laser light is split into a reference (25% power) and a sample path (75%) by a fiber coupler. Manual fiber polarization controllers are used in both paths for polarization matching.

The sample arm is comprised of a fiber collimator, a pair of galvanometers (6215H, Cambridge Technology, MA, US) in conjungated scanning configuration and a scan lens (AC508-075-C, Thorlabs, NJ, USA), focusing the beam into the sample.

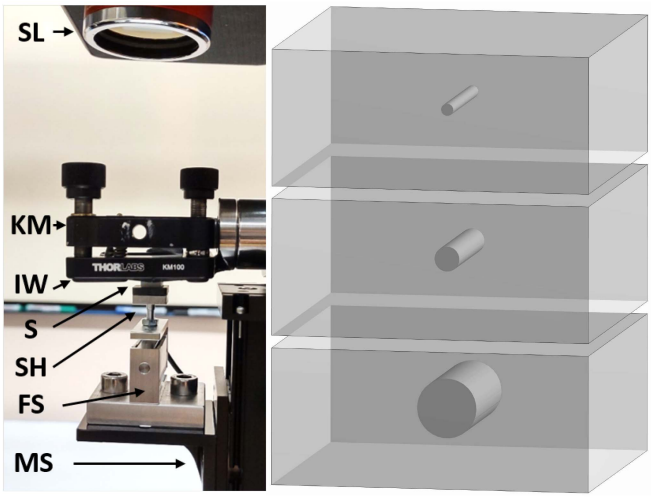

Fig. 2. (a) Automated Compression add-on to the OCT system: SL: OCT scan lens; KM: kinematic mount; IW: microscope slide used as imaging window, S: sample; SH: sample holder; FS: force sensor; MS: motorized stage. (b) Phantom Schematic. A $7 \times 7 \times 3\,\mathrm{mm}^3$ rectangular cuboid background material surrounds a cylindrical inclusion of $3\,\mathrm{mm}$ length and a small ($0.27\,\mathrm{mm}$), medium ($0.55\,\mathrm{mm}$) or large ($1.31\,\mathrm{mm}$) diameter.

The light scattered back inside the sample is collected by the collimator again, and guided through a circulator to a 50 - 50% fiber coupler, used for recombining both beam parts in Mach-Zehnder fashion. The reference arm is constructed similarly, but consists only of a collimator, a free space track and a reference mirror. To prevent oversaturation, the reference power can be dimmed using an attenuation wheel. After the light is recombined and split into two parts with equal intensity, it is captured by a dual balanced detector (BPD-1, Insight Photonic Solutions, CO, US). The dual balanced detector delivers an analogue signal, which is filtered using a 1.8 MHz highpass filter (EF509, Thorlabs, NJ, USA) and a 0.5–750 MHz bandpass filter (ZFHP-0R50-S, Mini-Circuits, NY, USA). All used fibers are single mode fibers.

The Insight swept source is controlled by a PC via an Ethernet cable and triggers the sample clock of the data acquisition card (ATS9360, Alazar Technologies Inc., QC, Canada), which is used to record the analogue signal and to deliver an A-line trigger to the field programmable gate array (FPGA, NI PCIe 7841R, National Instruments, TX, US) as well. The FPGA is programmed using LabView (2018, National Instruments, TX, US) to supply the galvanometer servo drivers with the driving voltage for the OCT scan pattern. The OCT control software was also programmed in LabView in-house. It yields an axial resolution of $27.3\,\mu\mathrm{m}$ and a lateral resolution of $22\,\mu\mathrm{m}$ in skin as well as in the phantom material used in this work. The axial field of view in air is $838\,\mu\mathrm{m}$.

B. Compression Setup

A compression add-on (see Fig. 2) for the OCT system was built, featuring automated uniaxial compression and precise, time-resolved force reading. A motorized stage (T-LSM050 A, Zaber Technologies, Vancouver, Canada) is used to compress the sample between a microscope slide and a S-shaped precision force sensor (KD34 s $\pm$10 N, ME-Systeme, Brandenburg, Germany). The microscope slide acts as an imaging window allowing the OCT illumination to reach the compressed sample. The stage achieves a minimal stepsize of $47.6\,\mathrm{nm}$ and can be easily controlled by manufacturer-provided functions. A maximum force of $25\,\mathrm{N}$ can be applied by the stage, while the force sensor's saturation is limited to 10 N. The sensor has a force precision of 0.1%. A custom made sample holder, which can be screwed into the sensor, was fabricated. It is composed of an aluminium corpus and a $2\,\mathrm{mm}$ layer of hard plastic covering. The plastic surface is visible in OCT, without being as reflective as the aluminium, therefore preventing imaging artefacts. While the stage features a USB cable to connect it to the PC for control and feedback, a connector plug was soldered to the bare litz wires of the sensor, for connecting it to the FPGA. An FPGA subroutine, parallel to the OCT acquisition control, reads out the force sensor continuously.

A LabView app, synchronizing OCT acquisition, compression and force recording was developed. The compression add-on was calibrated using a set of commercially available normed weights and showed a very linear force response (a Pearson's correlation coefficient of 0.9998) over the whole region of interest.

C. Phantoms

Twelve phantoms, featuring a soft, middle, or hard cylindrical inclusion of three different sizes, embedded in different background materials were produced (see Table III). Silicone elastomers are commonly used to test and develop OCE systems (e.g. [44], [45], [46]). They are easy to manufacture and are supposed to show only very little viscoelasticity [47]. For this work, "S10 slow," "S20" and "S30" of the Dragon Skin series from Smooth-On (TX, USA) were used. These silicone elastomers come as a kit of two separate, very viscose fluid components, which are mixed according to the datasheet. To enhance the feature density of the material in OCT, titatium dioxide particles, TiO_2 (37262-25 G, Sigma-Aldrich, CA, USA) were added to the mixture before curing. The TiO_2 has no defined particle size, leading to very distinct, highly scattering dots in the medium, but also to increased background scattering. The inclusions were fabricated via letting the silicone cure while being inside syringe needles of three different diameters and afterwards cutting off pieces of 3 mm length. The inclusion diameters were measured afterwards using OCT, yielding 0.27 mm for the small, 0.55 mm for the medium, and 1.31 mm for the large inclusion. The inclusion diameter measured in lateral direction fitted well to the inclusion diameter in axial direction with the refractive index of the material taken into account. These inclusions were then embedded into the background material and cured overnight. Since punching out pieces of silicone proved very unreliable, custom made aluminium and 3D printed polylactide (PLA) casting molds were used to shape the phantoms. Any residues from the casting process were cut off with a scalpel. All phantoms have a footprint of $7 \times 7\,\mathrm{mm}^2$ and a height of $3\,\mathrm{mm}$. Since the mechanical properties depend on the age of the silicone kit, the

exact mixing ratio, as well as on the exact amount of added TiO_2, every time a phantom part was produced, a homogeneous material piece which serves as a ground truth was simultaneously produced from the same mold.

These ground truth pieces were tested with OCE in order to determine their Young's moduli. The values resulting from the macroscopic analysis (Section II-F) are used as ground truth for all further analysis in this work. In general, there is one ground truth value for the "S20" and the "S30" material, one for all "S10" inclusions and one for all "S10" backgrounds. This is caused by the chronological order of their fabrication:

1) Fabrication of S10 inclusions;
2) Embedding of S10 inclusions into S20 and S30 background material. From the same batch S20 and S30 inclusions are fabricated;
3) S20 and S30 inclusions are embedded into newly mixed S10 background material.

The fabrication of the one phantom with small "S10" inclusion in "S20" background did not go as planed, therefore a replacement phantom was produced.

The group refractive index at 1300 nm was measured to be 1.405 for each individual phantom using OCT. Prior to OCE imaging, each phantom underwent 100 compression cycles of 1mm to reduce the Mullins effect [23].

D. Measurements

A manual precompression of about $1\,\mathrm{N}$ ensures that both upper and lower boundaries of the phantom are in full contact with the compression system. From this starting point, the phantom is compressed in 10 compression steps of about $40\,\mu\mathrm{m}$. Each compression step is kept constant for $5\,\mathrm{minutes}$ to let the sample reach a force equilibrium. After this relaxation time, a 3D OCT image is taken automatically. This procedure is repeated until ten tomograms of consecutive compression steps are acquired. The same measurement was performed for each ground truth piece.

Tomograms are taken with a field of view of $10 \times 10\,\mathrm{mm}^2$, corresponding to 1024×1024 pixels.

E. Image Processing

The following image processing steps were performed on all 12 inclusion phantoms for all three presented reconstruction methods as well as on all ground truth phantoms for determining the compression induced phantom size changes. OCT post-processing, i.e., the derivation of images from the recorded interference signal, and the image processing are performed in MATLAB (2021, MathWorks, MA, USA), partially using the GPU (Titan Xp, Nvidia, CA, USA) incorporated in the measurement control PC. The Insight laser control software, which accompanies the swept source, saves the valid data point position found during calibration in a text file. This valid data point mask is applied to the data, discarding all non-valid data points. Fourier transform yields the 3D OCT volume. No dispersion compensation is performed, because the bandwidth of the laser is barely $30\,\mathrm{nm}$ centered at $1300\,\mathrm{nm}$.

For the quasi-static, intensity-based, compression OCE approach, a semi-automatic data processing routine was developed. First, the spectral OCT data is converted to the image space, as is common for SD- and SS-OCT. Then, the 3D image of the sample is rotated to align with the image coordinate system. Three prominent planes appear in the OCT image: one corresponds to the sample holder - phantom interface, one to the microscope glass - phantom interface, and one to the sample holder - air interface. These planes were found and used for rotation, but also for determining the refractive index of the phantom. The air surrounding the phantom laterally is assumed to have a refractive index of 1. The geometrical distance between the compression plates is the same whether the light passed through the phantom or through the air surrounding it, but the optical distance changes with the refractive index. If the air is assumed to have a refractive index of 1, the refractive index of the material can be calculated. The refractive index of each phantom during each compression step was determined this way. No compression induced change in refractive index could be observed by the presented OCE system. Interpolation is used to achieve cubic voxel dimensions, taking the refractive index of the sample into account. The phantoms in these 3D images are aligned with the image coordinate system and the voxels have cubic dimensions.

F. Ground Truth

An engineering strain/stress approach was used to estimate the Young's modulus of each phantom material batch from the homogeneous ground truth pieces (the values are given in Table III). The stress acting on the phantom is calculated from the recorded force and the area upon which the force is applied ((1)).

$$\sigma_{ph}(ccs) = \frac{F(cs = 2...10) - F(cs = 1)}{A} \tag{1}$$

Since the force behavior is recorded during the whole relaxation time, the average over the last $0.3\,\mathrm{seconds}$ of the force reading was used as quantification of the force ($F(cs)$), for each compression step (cs). The difference in $F(cs)$ between all but the first compression steps to the first compression step is considered as the loading.

The area ($A(cs)$) is derived from the OCT images by segmenting the region where the sample touches the imaging window, using simple intensity based segmentation. Because the phantom sticks to the sample holder and the microscope slide, no relevant change of contact area can be observed. Therefore, the mean area A over all $A(cs)$ can be used to counteract possible segmentation issues. The sample height ($L_{ph}(cs)$) is determined by finding the distance between the imaging window and the compression plate in the OCT images. The change in phantom height was used to calculate the strain in between each compression step (2).

$$\epsilon_{ph}(ccs) = \frac{L_{ph}(cs = 2...10) - L_{ph}(cs = 1)}{L_{ph}(cs = 1)} \tag{2}$$

The obtained strain ϵ_{ph} and stress σ_{ph} values for each change between compression steps ($ccs = 1...9$) are fitted, and the resulting slope is considered as approximation of the Young's modulus of the sample (see Fig. 3). This approach neglects all non-homogeneities inside the phantom.

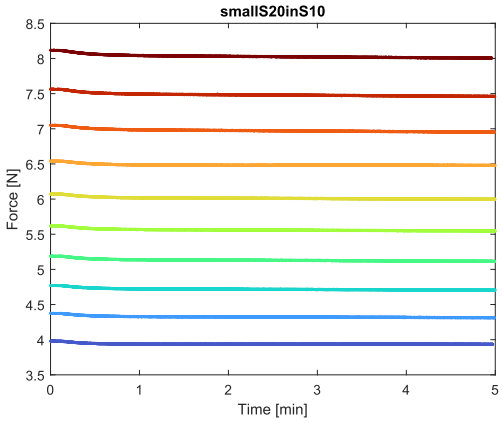

(a)

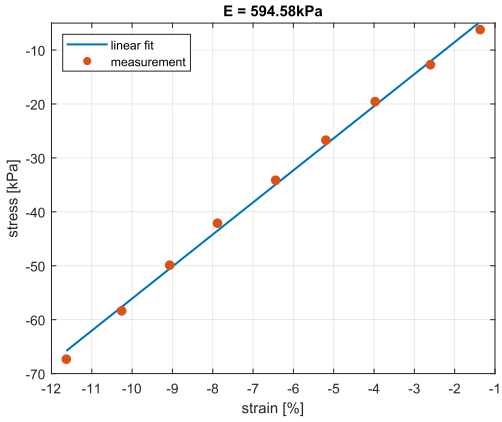

(b)

Fig. 3. Elastic behaviour of the phantoms for all 10 compression steps (from $cs = 1$ in blue at $\sim$4 N in consecutive order to $cs = 10$ in red at $\sim$8 N): (a) Within less then half a minute an equilibrium of forces is reached. (b) Stress and strain inside the phantom show a linear behavior for most of the measurement range.

TABLE I
COMPARISON OF RESULTS BY OCE TO COMMERCIAL TENSILE TESTING MACHINE (GOLD STANDARD)

Material (Abbreviation)	**Young's Modulus [kPa]**			
	OCE		TA Instrum.	
	mean	std	mean	std
S10	642	18	623	19
S20	1001	18	952	42
S30	1382	48	1355	32

1) Ground Truth Validation: To validate this method, a comparison measurement utilizing a tensile testing machine consisting of a 200 N ElectroForce testbench system (TA Instruments, New Castle, DE, USA) and a 10 N load cell (Model WMCP-1000 g, Interface Inc., AZ, USA) was performed. Since the mechanical parameters of the silicone elastomer phantoms change over time, an additional set of homogenous phantoms was produced for this comparison, to ensure timely measurements. To minimize Mullin's effect, each phantom was first compressed 100 times for 1 mm. The TA Instruments measurement was always performed right before the OCE measurement. The results in Fig. 4 and Table I show that our method of determining

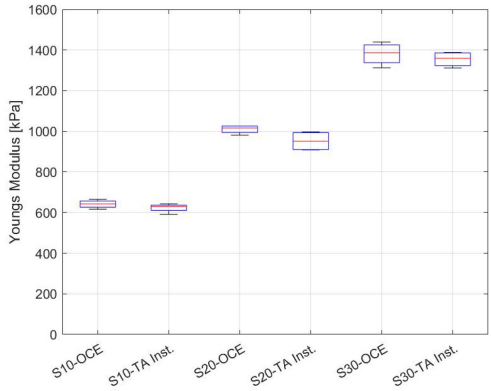

Fig. 4. The macroscopic Young's modulus values found from OCE are in good agreement with the results from a TA Instruments tensile testing machine. Each box of the boxplot covers four phantoms from a single material batch.

the ground truth is in accordance with the results achieved by the commercially available TA Instruments tensile testing machine.

G. 3D to 2D Projection

The following image processing steps are performed on all 12 inclusion phantoms and are necessary for all three reconstruction methods. While the 1D analysis and the intensity-based inversion method use only the segmentation maps as inputs, the particle tracking improved optical flow uses the segmentation map to enhance the image contrast. Even though the TiO_2 particles provide increased information density, a lateral projection to 2D was necessary to achieve a sufficiently high density for further analysis.

The 3D images are generously cut in lateral direction to remove any non-phantom regions. On the lateral boundaries the phantom is in contact with air. These boundaries are close to being parallel to the optical beam, producing undesired artefacts in the OCT image, due to Snell's law. In axial direction, everything above the glass - phantom plane is removed. In addition to the phantom region, a part of the sample holder region is kept to ensure that the images have the same dimensions for all compression states. The light intensity distribution inside a sample in OCT is not homogeneous by nature. The intensity of a sample feature in OCT depends on its distance to the optical focus and its depth position. The location of the TiO_2 particles in the presented phantoms are moved by the compression with respect to the focus and their depth inside the phantom material is changed. These effects lead to brightness changes of the TiO_2 particles in OCT tomograms recorded during consecutive compression steps. The optical flow, which is applied later for inferring the motion, depends on stable feature intensities. To compensate for these OCT-induced intensity changes, an image intensity homogenization step is performed. The average depth profile of the image data cube is subtracted from the data cube itself.

A maximum intensity projection (MIP) was used to convert the data region of interest from 3D to 2D. For this, several slices from the center of the phantom were selected, leveraging the symmetric geometry of the experiment and projecting the

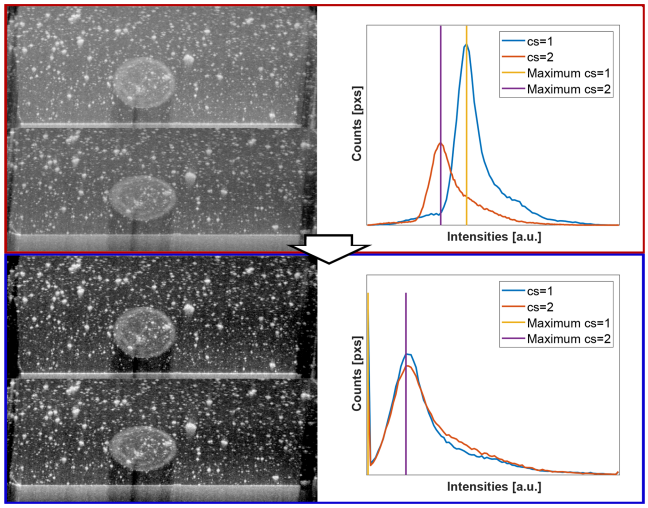

Fig. 5. Adjusting the intensity between consecutive compression steps. The top row (red frame) shows the MIP of two compression steps and their histogram. The histograms are modified so that their maxima are overlapping (blue frame). The lateral phantom boundaries cannot be imaged perfectly, due to the phantom's high refractive index ($n_g = 1.405$) and parallelism to the illumination.

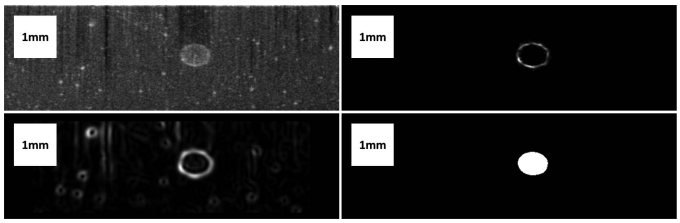

Fig. 6. The Inclusion area was segmented using a semi-automated two-step gradient based approach: First, the rough outlines of the inclusion are found. Then, only the outline region is used to precisely determine the inclusion boundaries.

cylindrical inclusion to a circle. The amount of slices was chosen based on the slight inclination of the inclusion in each sample, ensuring that the projection is reasonable. The histogram of the 2D MIP does not correspond to the histogram of the 3D image, and also the comparability of the image intensities between compression steps is lost through the MIP. Therefore, the intensities were matched after the projection. The highest and lowest intensity values of the image were chosen in such a way that the most common intensities of all compression steps have the same value (see Fig. 5).

For further analysis, the images were segmented into the area of the inclusion and the area of the background (see Fig. 6). For this, an average intensity projection (AIP) over the same selected slices was used. This projection enhances the difference in brightness between inclusion and background but diminishes the particle brightness. A semi-automatic two-step gradient-based algorithm was developed for the segmentation. First, a highly Gaussian smoothed image was used to find the inclusion location. Then, an only slightly smoothed image was used to determine the course of the inclusion boundary. This segmentation mask was directly used as input for the 1D analysis as well as for IIM. For EOFM the segmentation mask was used for brightness adjustment and finally to estimate the inclusion and background stiffness from the strain maps.

H. 1D Stiffness Analysis

Under the assumption of a homogeneous stress distribution throughout the phantom, the Young's modulus of inclusion and background can be derived from the deformation of the segmentation mask in between the compression steps. This approach neglects any side-wards expansion of the phantom, as well as any effect of the non-homogeneous nature of the phantom. Each cross-section (with index x) in compression direction is analysed separately. The 2D segmentation masks of the first ($cs = 1$) and the last ($cs = 10$) compression step are considered and using them, the movement of the inclusion boundaries (z_b, z_c) and the phantom boundaries (z_a, z_d) are tracked. From the boundaries, the height of the inclusion and the background are calculated:

$$L_{incl}(x, cs) = z_c(x, cs) - z_b(x, cs)$$
$$L_{bg}(x, cs) = z_b(x, cs) - z_a(x, cs) + z_d(x, cs) - z_c(yx, cs).$$

The strain ($\epsilon_{incl}(x)$ and $\epsilon_{bg}(x)$) and the Young's modulus for inclusion ($E_{incl}(x)$) and background ($E_{bg}(x)$) are calculated (3):

$$\epsilon_{incl}(x) = \frac{L_{incl}(x, cs = 10) - L_{incl}(x, cs = 1)}{L_{incl}(x, cs = 10)}$$
$$\epsilon_{bg}(x) = \frac{L_{bg}(x, cs = 10) - L_{bg}(x, cs = 1)}{L_{bg}(x, cs = 10)}$$
$$E_{incl}(x) = \frac{\sigma}{\epsilon_{incl}(x)}; \quad E_{bg}(x) = \frac{\sigma}{\epsilon_{bg}(x)}; \tag{3}$$

The best precision is achieved if the displacement is as large as possible compared to the discretization error, while still within the linear elastic range of the phantom. Therefore, in the uniaxial analysis the largest available displacement between the first ($cs = 1$) and the last compression step ($cs = 10$) is considered.

For the Young's modulus values provided in Section III-B, the average over a 10 pixel region in the center of the inclusion (x_c) is depicted (Fig. 7 and (4)). The lateral border region of the inclusion is not considered, to avoid dividing through a very small inclusion height.

$$E^{av}_{incl} = \sum_{x=x_c-5}^{x_c+5} E_{incl}(x); \quad E^{av}_{bg} = \sum_{x=x_c-5}^{x_c+5} E_{bg}(x); \tag{4}$$

I. Particle Tracking Improved Optical Flow for 2D Stiffness Analysis

For estimating the internal displacement field arising inside the sample during compression, we use our recently developed Elastographic Optical Flow (EOFM) method [43]. This method is based on the classic optical flow equation

$$I_t + \nabla I \cdot \mathbf{u} = 0\,, \qquad \forall\, t \geq 0\,, \tag{5}$$

which connects an image intensity function $I = I(\mathbf{x}, t)$ with a displacement field $\mathbf{u}(\mathbf{x}) = (u_1(\mathbf{x}), u_2(\mathbf{x}))$ for $\mathbf{x} \in \Omega \subset \mathbb{R}^2$. Based on the well-known Horn-Schunck method (references as

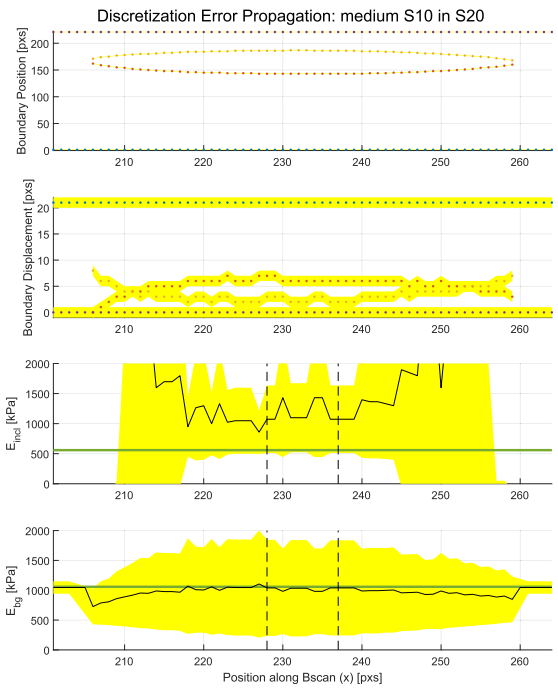

Fig. 7. Propagation of the image discretization error. The ± 0.5 pixel error of the boundary discretization leads to a huge uncertainty in the reconstruction of the Young's modulus if only the displacement in compression direction is considered. The error is depicted in yellow. Top to bottom: ± 0.5 pixel boundary location error; ± 1 pixel error in the displacement; the error of the inclusion's Young's modulus rises sharply at the lateral inclusion boundaries, because of the division through a very small inclusion thickness value, with a comparably high error; background Young's modulus with error. The dashed lines mark the region used for the averaged values in Table III and the green line marks the ground truth.

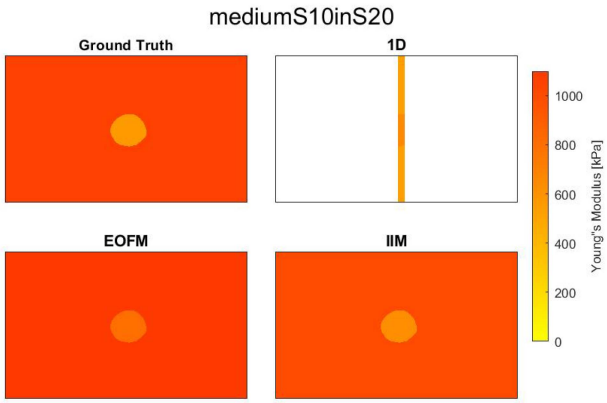

Fig. 8. Young's modulus maps of a S20 phantom with a medium S10 inclusion. The ground truth was derived from homogeneous phantoms. For the 1D results the Young's modulus of a thin region in the center of the inclusion was selected, because the influence of the discretization error is stronger at the lateral inclusion borders. The EOFM results are calculated with a uniform stress assumption from the strain maps derived by EOFM. The IIM results are close to the ground truth results.

standard OF), EOFM produces an improved displacement field estimate by using

1) physically meaningful boundary conditions,
2) particle tracking based displacement information,
3) physically motivated background information.

The use of this prior information in EOFM helps to overcome the observed non-physicality of displacement and strain resulting from standard methods. We now provide a practical step-by-step outline of EOFM, and refer to [42], [43] for the derivation and mathematical analysis.

Step 1: In this step, we extract additional displacement information from the OCT scans for our method. For this, we detect the locations $\hat{\mathbf{x}}^i = (\hat{x}_1^i, \hat{x}_2^i) \in \mathbb{R}^2$, $i = 1, \ldots, M$, of a total number M of particles in the initial OCT scan and track their movement between consecutive OCT scans during compression. This was done with our heuristics-based image-processing algorithm recently introduced in [42]. We save the movement of each tracked particle in the displacement vectors $\hat{\mathbf{u}}^i = (\hat{u}_i^1, \hat{u}_i^2) \in \mathbb{R}^2$, $i = 1, \ldots, M$.

Step 2: Next, we compute a background field $\mathbf{u}^{bg}$ which serves as a-priori information for the computation of $\mathbf{u}$ below. We do this in the following way: we take an estimate of the Young's modulus E^{bg} and the Poisson ratio ν^{bg} of the background material of the sample. Then, we model an inclusion-free sample with these material parameters and the same overall geometry as the sample with inclusion. Next, we simulate the movement of this sample when it undergoes the same compression as in the OCE experiments for the sample with inclusion. For this, the equations of linearized elasticity are solved together with physically meaningful boundary conditions. In our experiments, we use constant Dirichlet conditions corresponding to the fixed and compressed sides of the sample, as well as homogeneous Neumann conditions on the traction-free sides of the sample. Finally, we save the modeled movement into the displacement field $\mathbf{u}^{bg}(\mathbf{x})$.

Step 3: We pre-process the OCT images for displacement field estimation by adjusting their brightness using the segmentation map, applying an appropriate smoothness filter, and potentially also by cutting off imprecise edge measurements.

Step 4: In order to compute the final displacement field $\mathbf{u}$, the background field $\mathbf{u}^{bg}$ has to be amended by an update field $\mathbf{u}^{upd}(\mathbf{x}) = (u_1^{upd}(\mathbf{x}), u_2^{upd}(\mathbf{x}))$ via $\mathbf{u} = \mathbf{u}^{bg} + \mathbf{u}^{upd}$. Since $\mathbf{u}$ has to satisfy the optical flow (5), $\mathbf{u}^{upd}$ has to satisfy

$$I_t + \nabla I \cdot \mathbf{u}^{upd} + \nabla I \cdot \mathbf{u}^{bg} = 0\,. \tag{6}$$

We now want to compute $\mathbf{u}^{upd}$ from this equation, which as for standard optical flow requires the use of a-priori information. As stated before, in EOFM the following a-priori information extracted in the previous steps is used: The locations $\hat{\mathbf{x}}^i$ and the displacements $\hat{\mathbf{u}}^i$ of the tracked particles, the background field $\mathbf{u}^{upd}$, the assumption of smoothness of the displacement field $\mathbf{u}$, as well as physically motivated boundary conditions. Hence, following [42], [43] we now compute the update field $\mathbf{u}^{upd}$ as the minimizer of the functional

$$F(\mathbf{u}^{upd}) := \int_\Omega \left(I_t + \nabla I \cdot \mathbf{u}^{upd} + \nabla I \cdot \mathbf{u}^{bg}\right)^2 d\mathbf{x} + \alpha \int_\Omega \left|\nabla u_1^{upd}\right|^2 + \left|\nabla u_2^{upd}\right|^2 d\mathbf{x}$$

$$+\beta\sum_{i=1}^{n}\int_{\Omega} g_\sigma(\mathbf{x},\hat{\mathbf{x}}^i)\left|\mathbf{u}^{upd}+\mathbf{u}^{bg}-\hat{\mathbf{u}}^i\right|^2 d\mathbf{x}\,, \tag{7}$$

where $g_\sigma(\mathbf{x},\hat{\mathbf{x}}^i)$ is a Gaussian function with standard deviation σ centered around $\hat{\mathbf{x}}^i$. For minimizing $F(\mathbf{u}^{upd})$, we follow an idea of Schnörr [48] adapted for EOFM in [43]: namely that under rather mild mathematical assumptions, the minimizer of $F(\mathbf{u}^{upd})$ is given as the unique solution of a linear variational problem. After discretization using a finite element approach, we thus find $\mathbf{u}^{upd}$ by solving a linear system of equations; see [43] for details.

Note for completeness that mathematically, the minimization of $F(\mathbf{u}^{upd})$ needs to be performed over a suitable function space which incorporates physically meaningful boundary conditions. Since for our experiments these are already encoded in the background field $\mathbf{u}^{bg}$, the minimization is carried out over all sufficiently smooth functions satisfying zero Dirichlet boundary conditions on the top and bottom of the sample.

Step 5: Finally, we compute the displacement field $\mathbf{u}$ via

$$\mathbf{u}=\mathbf{u}^{bg}+\mathbf{u}^{upd}\,, \tag{8}$$

i.e., by adding the background and update fields $\mathbf{u}^{bg}$ and $\mathbf{u}^{upd}$.

For evaluating the quality of the resulting EOFM displacement field, we calculate the approximate relative error as $\text{err}=\|\mathbf{u}-\mathbf{u}^{model}(E_{incl},E_{bg})\|_2/\|\mathbf{u}^{model}(E_{incl},E_{bg})\|_2$, where $\mathbf{u}^{model}(E_{incl},E_{bg})$ is the expected field derived using the elastic model with the ground truth values (E_{incl},E_{bg}) and the segmentation map of the sample available from the image processing step. All components of the error are calculated on the pixel-size discretization of the sample and the standard 2-norm is taken from the spatially varying vector displacements.

Since the stress distribution inside the sample is unknown, the uniform stress assumption is used to calculate the Young's modulus from the derived strain maps. This assumption neglects the impact of the inclusion on the stress map, as well as any boundary effects. The compression force recorded during measurement is divided by the sample's contact area with the compression system (Section II-F) to derive the uniform stress. This stress is then divided by the strain delivered by EOFM at each pixel position to get a Young's modulus map. For comparison with the other methods, the segmentation mask (Section II-G) was applied, and the mean and standard deviation of the Young's modulus of both the inclusion the and background were derived.

J. Intensity-Based Inversion Method for 2D Stiffness Analysis

The intensity-based inversion method (IIM) is a novel approach for reconstructing the unknown material parameter E by solving an intensity-based inverse problem for both E and ν. This way the lateral sample expansion is taken into account as well, without the need for any assumptions concerning the compressibility of the sample.

The starting point of the method is the relation

$$I_1(\mathbf{x}+\mathbf{u}(E(\mathbf{x}),\nu(\mathbf{x})))=I_2(\mathbf{x})\,, \tag{9}$$

which connects the OCT intensities I_1 and I_2 of two compression states of the sample via a deformation model (linear elasticity) expressed by the displacement $\mathbf{u}$ in dependence on E and ν. We want to compute E and ν from (9), which requires regularization similar to the Horn-Schunck method. Hence, in IIM we estimate E and ν by minimizing the functional

$$G(E,\nu):=\int_{\Omega}\left(I_1(\mathbf{x}+\mathbf{u}(E(\mathbf{x}),\nu(\mathbf{x})))-I_2(\mathbf{x})\right)^2 d\mathbf{x} + \alpha\int_{\Omega}|E(\mathbf{x})|^2+|\nu(\mathbf{x})|^2\,d\mathbf{x}\,, \tag{10}$$

where α is a regularization parameter regulating the smoothness of the obtained estimate. In our experiments, we use $\alpha=10^{-3}$ in order to avoid oversmoothing.

For the minimization of the functional G, we use an alternating direction version of the Nelder-Mead method [49], also known as the downhill simplex method. This is a direct search optimization method based purely on comparisons between function values, and without the need to compute any derivatives. In IIM, we apply the Nelder-Mead method in an alternating direction fashion to the components of the functional G. More precisely, we first fix some initial estimate of the Young's modulus E, and then estimate the Poisson's ratio ν. Then, we fix the resulting estimate of ν and minimize the functional G with respect to the parameter E. We continue in this alternating way until the difference of the value of G between two consecutive iterations reaches a tolerance of 10^{-6}, typically after a couple of hundreds of iterations.

For the numerical implementation of the alternating direction Nelder-Mead method, we need to provide a numerical routine for evaluating the functional G at any parameters E and ν. To do so, we need to compute $I_1(x+\mathbf{u}(E(x),\nu(x)))$, which is done in the following way: First, we compute the displacement field $\mathbf{u}(E,\nu)$ via the linear elasticity model. Then, we use it to deform I_1 via a pixel-grid deformation with the field $\mathbf{u}$. Note that this approach is not limited to the model of linear elasticity used here, but can also be applied with any deformation model suitable for a specific experiment.

Note that the minimization of G can also be accomplished using any other suitable optimization algorithm of choice. E.g., one can use any gradient-free, first or second order gradient method, since with our choice of the linear elasticity model connecting $\mathbf{u}$ and E,ν, the gradient of G can be calculated explicitly. However, the numerical computation of this gradient is sensitive to noise in the OCT images I_1 and I_2, which is why we use the gradient-free Nelder-Mead method in IIM.

Since a segmentation of the sample is available from the processing step, we make use of this additional information to reduce the dimensionality of the inverse problem by decomposing the sample into the inclusion and background areas, Ω_{incl} and Ω_{bg}, and searching for the corresponding unknown values of E and ν per area. This is implemented via describing the material parameters as piece-wise constant functions

$$E(\mathbf{x})=E_{incl}\chi_{\Omega_{incl}}(\mathbf{x})+E_{bg}\chi_{\Omega_{bg}}(\mathbf{x}), \tag{11}$$

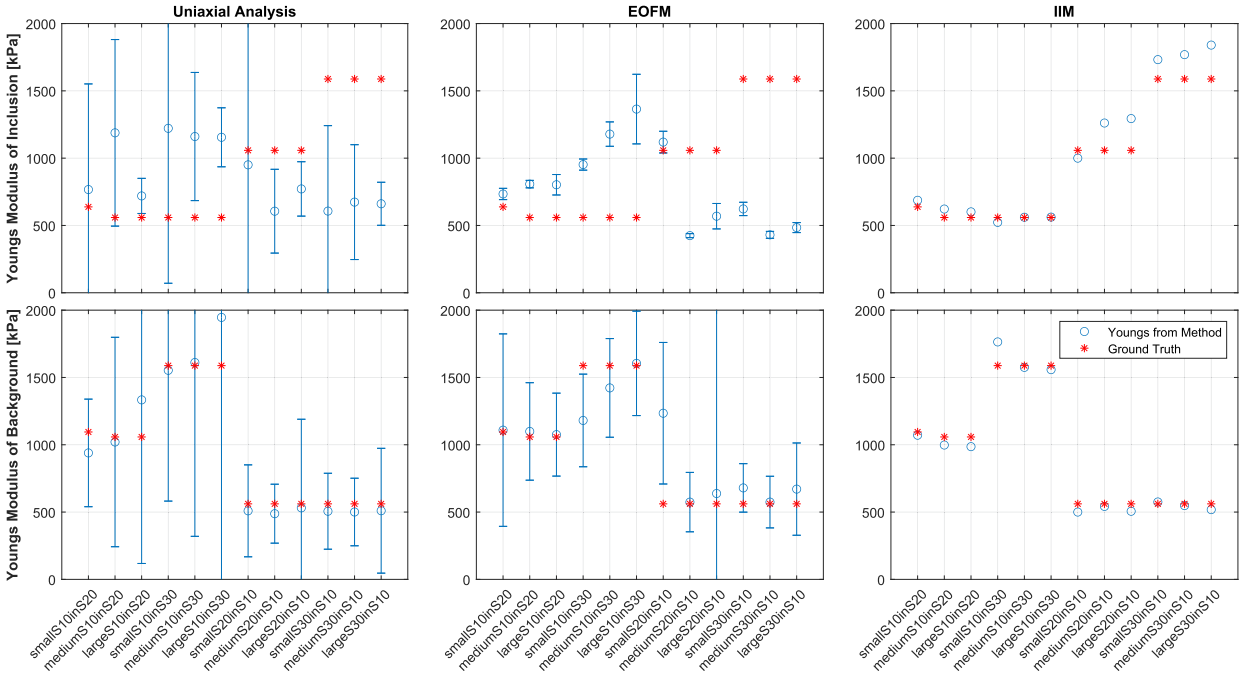

Fig. 9. Comparison of the results from all three methods. The blue circles mark the values derived using 1D analysis, EOFM strain maps and IIM. Note that the errorbars are derived differently. The error for the 1D analysis was found via error propagation and depicts only the discretization error. The errorbars for the strain map based reconstruction is the standard deviation over the segmented element. For IIM it is not possible to give a good approximation for the error. For a complete description consult Section II-H, Section II-I and Section II-J. The red asterisks mark the ground truth.

$$\nu(\mathbf{x}) = \nu_{incl}\chi_{\Omega_{incl}}(\mathbf{x}) + \nu_{bg}\chi_{\Omega_{bg}}(\mathbf{x}), \tag{12}$$

with the indicator functions $\chi_{\Omega_{incl}}$ and $\chi_{\Omega_{bg}}$ for the areas and E_{incl}, E_{bg}, ν_{incl}, ν_{bg} for the unknown values. Hence, in our experiments we determine four parameters for each sample. To start the IIM algorithm in this case, an initial guess (E_0, ν_0) is required for the Poisson's ratio and Young's modulus. We chose $\nu_0 = 0.45$ for both inclusion and background values and a rough guess to the background for E_0 for all samples.

Note that IIM can be applied to any general material parameter functions and is not limited to the simplified problem relying on the segmentation.

III. Results and Discussion

Fig. 8 shows a comparison of the Young's modulus that were derived via the three presented methods for a phantom made out of S20 material with a softer S10 inclusion.

A. Elastic Sample Behavior

The silicone elastomer phantoms are a very good choice for mimicking elastic behavior. They need less than 30 seconds to reach force equilibrium if a constant compression distance is applied, indicating their non-viscosity. In Fig. 3 (top), the force required to keep a certain constant compression is visualized over 5 minutes for 10 consecutive compression steps. The strain-stress relationship in the chosen strain region of interest (0 to ∼12%) shows a linear behavior (Fig. 3 (bottom)).

B. One Dimensional Results

The one dimensional analysis (Section II-H) could, for all but one phantom, determine whether the inclusion or the background has a higher stiffness (see Fig. 9). The quantitative results for the background values are well within their discretization error. The results for the inclusions are far off from the ground truth. While the relative errors of the background Young's modulus is well within 26.0% for all phantoms, the relative error of the inclusion values go up to 118.5%.

This can be explained by an accumulation of errors: When detecting a phantom or inclusion boundary, an error of ± 0.5 pixels is made. Through error margin propagation, this small error has a huge impact on the precision of the Young's modulus derived from it, as can be seen in Fig. 7.

To exemplify this, the error margin derivation for the phantom with small S10 inclusion embedded in S30 is presented in detail. First, consider the discretization error of the phantom part boundaries:

$$\Delta z = \Delta z_a = \Delta z_b = \Delta z_c = \Delta z_d = 0.5\,. \tag{13}$$

Using the method of error propagation the relative error margins of the strain can be expressed in terms of the discretization error:

$$\begin{aligned} \frac{\Delta\epsilon_{incl}}{\epsilon_{incl}} &= \frac{4\cdot\Delta z}{L_{incl}(cs=1) - L_{incl}(cs=10)} + \frac{2\cdot\Delta z}{L_{incl}(cs=1)}\,, \\ \frac{\Delta\epsilon_{bg}}{\epsilon_{bg}} &= \frac{8\cdot\Delta z}{L_{bg}(cs=1) - L_{bg}(cs=10)} + \frac{4\cdot\Delta z}{L_{bg}(cs=1)}\,. \end{aligned} \tag{14}$$

Since the background consists of two separated pieces in this one dimensional description, the discretization error affects the background error margins twice as often as the inclusion. Finally, the error margin of the Young's modulus can be formulated. Note that due to the homogeneous stress assumption only one stress value is considered for the inclusion as well as the background.

$$\Delta E_{incl} = \left|\frac{E_{incl}}{\sigma}\right| \cdot \Delta\sigma + \left|\frac{E_{incl}}{\epsilon_{incl}}\right| \cdot \Delta\epsilon_{incl} \approx \left|\frac{E_{incl}}{\epsilon_{incl}}\right| \cdot \Delta\epsilon_{incl}\,,$$
$$\Delta E_{bg} = \left|\frac{E_{bg}}{\sigma}\right| \cdot \Delta\sigma + \left|\frac{E_{bg}}{\epsilon_{bg}}\right| \cdot \Delta\epsilon_{bg} \approx \left|\frac{E_{bg}}{\epsilon_{bg}}\right| \cdot \Delta\epsilon_{bg}\,. \tag{15}$$

The error of the stress can be neglect, because it depends on the force sensor, which has a comparably high precision, and on the precision of the area upon which the force acts. While the size of this area is found using OCT and therefore also suffers from discretization, the large size of the area makes its error negligibly small. E.g., for a vertical line through the inclusion of the phantom with small S10 inclusion embedded in S30 we find the inclusion and background phantom segment lengths to be $L_{incl}(cs = 1) = 23\ pxs$, $L_{incl}(cs = 10) = 21\ pxs$, $L_{bg}(cs = 1) = 202\ pxs$ and $L_{bg}(cs = 10) = 185\ pxs$, leading to a strain of $\epsilon_{incl} = 0.0870$ and $\epsilon_{bg} = 0.0842$, with error margins of $\Delta\epsilon_{incl} = 0.0907$ and $\Delta\epsilon_{bg} = 0.0206$, respectively. The resulting relative error margins for the Young's moduli are $\Delta E_{incl}/E_{incl} = 104.4\%$ and $\Delta E_{bg}/E_{bg} = 24.5\%$. The size of the estimated relative error margin depends on the size of the inclusion as well as on the inclusion and background material, and is depicted as error bars in Fig. 9 for all investigated phantoms.

Another inaccuracy develops from the non-centered location of the inclusion with respect to the phantom. The presented analysis compares the change in inclusion height without taking into account the lateral movement of the inclusion due to the compression. Another error source is the uniform stress assumption, which is certainly not true for inhomogenous and anisotropic samples. The uniform stress assumption also neglects any boundary effects. Since most of the phantom volume consists of the background material, the background dominates the force needed to keep a certain compression. Therefore, the assumed uniform stress value is closer to the real stress experienced by the background than the real stress experienced by the inclusion.

If the Young's modulus of the inclusion is to be extracted quantitatively, a more sophisticated method needs to be used.

C. Elastographic Optical Flow Method (EOFM)

To include the information provided by the lateral sample motion a strain map based approach to the Young's modulus was considered. The strain maps where derived using EOFM, which allows for a physically plausible reconstruction of the displacement due to taking into account the particle tracking information and expected background motion. The results are less affected by the image resolution, since the 2D image is considered, and the derived displacement maps show sub-pixel resolution.

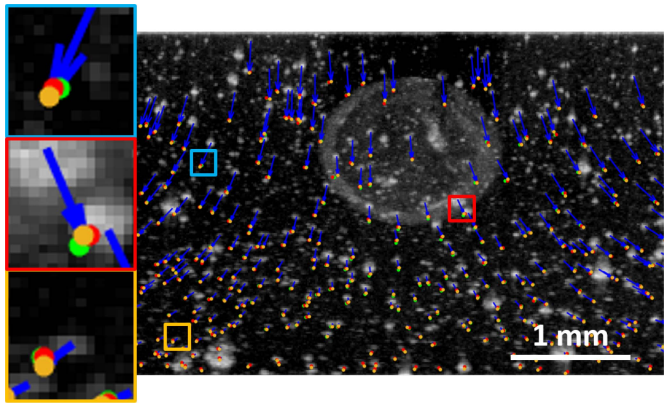

Fig. 10. An overlay of the particle movement captured by the particle tracking (yellow dots), the simulated movement of the particles (green dots) and the simulated movement of the particles in case the phantom was homogeneous (red dots). The image in the background depicts the first compression state $cs = 1$ and the blue arrows link the particles visible in the image to the particle movement endpoints $cs = 10$ from particle tracking. Color-coded squares show zoomed-in version of selected sample regions.

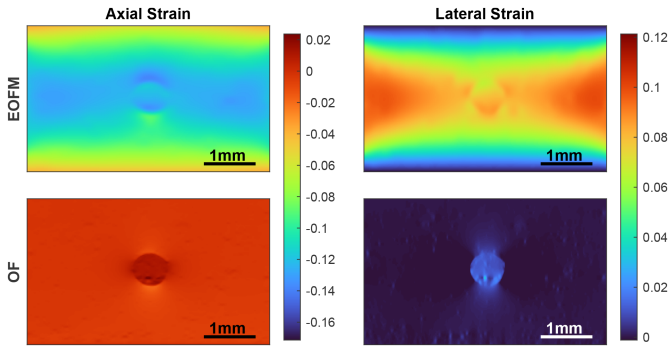

Fig. 11. A comparison with a standard Horn-Schunck optical flow method [39] shows that OF is capable of detecting the inclusion, but completely misjudges the background movement. EOFM is capable of correctly quantifying the background as well as the inclusion displacement, leading to a valid strain map.

The properties of EOFM were already discussed in detail in [43] and summarized in Section II-I. Hence, we only mention the following points here:

1) The use of information from particle tracking is one of the key-points which allows EOFM to obtain physically meaningful displacement field estimates of high quality. In turn, the precision of the particle tracking algorithm is important for the overall performance of the method (see Fig. 10).
2) In general, it is sufficient for EOFM if the values of E^{bg} and ν^{bg} are only approximately known. However, it is important to properly set the boundary conditions for the computation of $\mathbf{u}^{bg}$. This in turn requires a precise knowledge/measurement of the applied compression.
3) EOFM was shown to produce physically meaningful displacement field estimates of high quality, in particular when compared to standard optical flow techniques. In this context, note that while phase-sensitive OCT can be used to directly measure the axial component of the displacement field, techniques like EOFM reconstruct the full field,

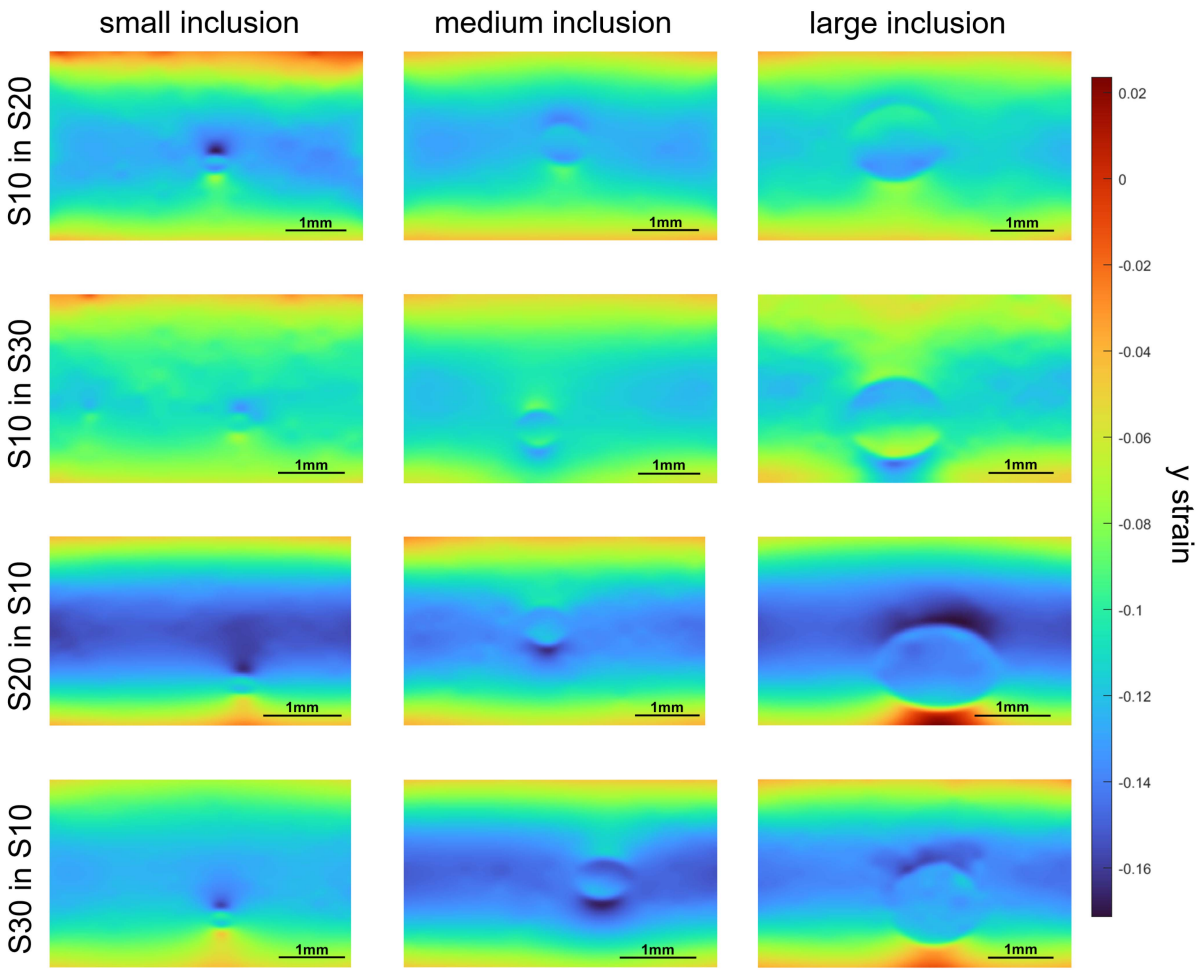

Fig. 12. Axial component of the strain maps calculated from EOFM displacement fields. Even the small inclusions can be spotted easily in the strain maps. The pixels are quadratic, making the scalebar valid for axial and lateral direction. The colorbars are scaled the same way for all phantoms for better comparability.

TABLE II
APPROXIMATE RELATIVE ERROR OF THE DISPLACEMENT DERIVED BY EOFM

Sample variant (Abbreviation)	**Displacement Error Approx. [%]** inclusion size		
	small (0.27 mm)	medium (0.55 mm)	large (1.31 mm)
S10 in S20	6.407	1.869	2.029
S10 in S30	7.772	3.418	4.535
S20 in S10	2.235	2.688	3.771
S30 in S10	4.170	2.512	5.067

i.e., including the lateral motion, which is necessary for recovering the material parameters, as was shown in [50].

4) Numerical experiments have shown a good agreement of EOFM displacement field estimates to those predicted by mathematical models of (linearized) elasticity (see Table II).

The EOFM approach is by far superior to the standard optical flow. To exemplify this, we include one reconstruction using the Horn-Schunck standard OF [39] and compare it to the EOFM result, see Fig. 11 (the strains are depicted for better visualization). Clearly, EOFM uses the particle tracking information to help the standard OF to catch the background movement. In Table II, the EOFM displacements are compared to the expected fields for the respective samples in terms of an approximate relative error, see Section II-I for details. Recall that the expected fields, i.e., "the ground truth displacements," are computed using the elastic model with the material ground truth values and the segmentation maps of the samples. Optical flow methods in general depend on stable feature intensities between consecutive images. While the used OCT setup provides a constant illumination intensity, the compression of the sample can induce some changes in the feature intensities. This fact, together with the variation in particle density from one phantom to another, poses an additional challenge in acquiring high precision results. Thanks to the particle movement being used as a second source of information, EOFM delivers physically plausible results where the experimental conditions would not allow for reasonable OF results.

A comparison of the particle movement detected in the images with the modelled particle movement indicates that pure feature tracking is not sufficient for finding the displacement. Fig. 10 compares the particle movement found through OCE (blue arrows with yellow dots) with the particle movement modeled for a phantom with inclusion (green dots) as well as for an inclusion-free phantom (red dots). The blue arrow marks where the particle shown in the image moves due to compression.

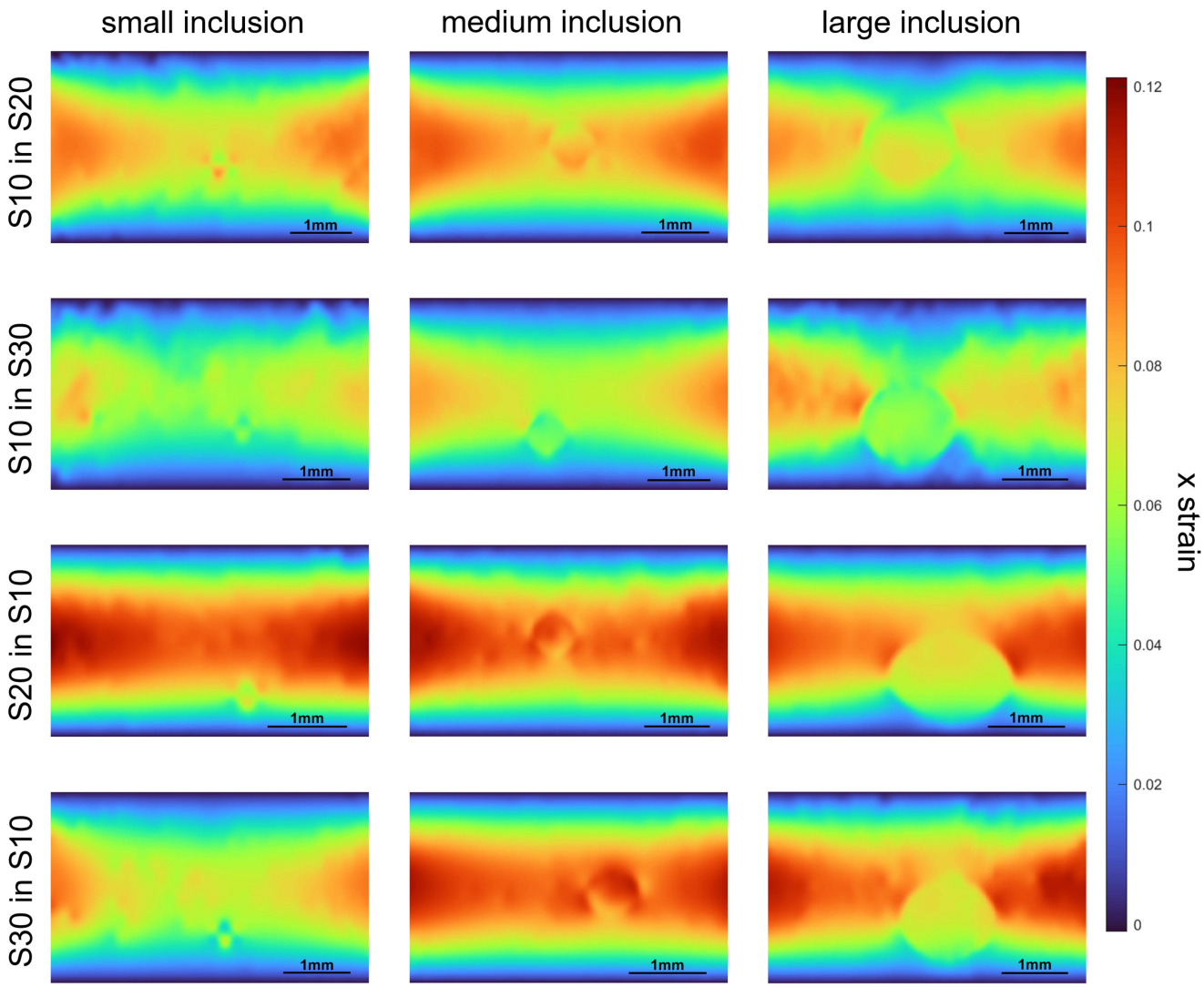

Fig. 13. Lateral component of the strain maps calculated from EOFM displacement fields. The strain maps are visualized with quadratic pixels and the scalebar is valid for the axial and lateral direction. The top and bottom of the phantom sticks to the compression device, preventing any lateral movement. This is reflected by the top and bottom boundaries of the strain map being zero.

The yellow dot marks the endpoint of this movement, while the red and the green dot mark alternative endpoints found through the respective model. The modeled particle movement is very similar to the modeled particle movement for an inclusion-free phantom. This shows that the effect of the presence of an inclusion on the particle movement is tiny. Hence, the particle movement found in the experiment does not by itself allow to distinguish between the homogeneous and non-homogeneous case, and the sparsity of the feature tracking data adds another difficulty.

Finally, note that structural symmetry of the sample can be leveraged for EOFM. For example, the samples used in our experiments are structurally uniform in the central part along their inclusion. Hence, a maximum-intensity projection can be performed over multiple image slices in that region, which increases the number of speckles available for detection and tracking, and thereby also the overall performance of EOFM.

From the resulting displacement map, the strain maps in axial (Fig. 12) and lateral (Fig. 13) direction are derived for all samples. Both the shape and size of the inclusions in various samples are clearly visualized by the strain results. For the sake of comparison, the colormaps for the strain values are scaled the same. Also, in order to remove the typical numerical singularities which propagate into the displacement solutions from the corners, a region of interest smaller than the original image is depicted. These singularities result from the boundary conditions of the involved equations changing their type at the image corners. The low lateral strain at the top and bottom phantom boundaries indicate the fixed boundary conditions. This assumption relates well to the fact that the silicone phantom material sticks to the glass slide as well as to the sample holder surface.

Using again the uniform stress assumption, the Young's modulus of both inclusion and background can be estimated (Fig. 9).

TABLE III
YOUNG'S MODULUS RECONSTRUCTED BY THE PRESENTED METHODS

Sample variant (Abbreviation)	**Young's modulus [kPa]** inclusion size					
	small (0.27 mm)		medium (0.55 mm)		large (1.31 mm)	
	inclusion	background	inclusion	background	inclusion	background
	Ground truth					
S10 in S20	638	1095	559	1058	559	1058
S10 in S30	559	1588	559	1588	559	1588
S20 in S10	1058	561	1058	561	1058	561
S30 in S10	1588	561	1588	561	1588	561
	1D analysis					
S10 in S20	451	526	649	526	423	725
S10 in S30	525	588	486	675	454	702
S20 in S10	776	392	613	465	572	355
S30 in S10	591	467	613	424	596	425
	EOFM					
S10 in S20	734	1109	807	1099	802	1075
S10 in S30	952	1181	1179	1422	1365	1605
S20 in S10	1119	1234	424	574	569	638
S30 in S10	623	680	430	574	484	671
	IIM					
S10 in S20	687	1071	622	998	601	986
S10 in S30	523	1764	561	1575	562	1558
S20 in S10	1000	500	1261	542	1294	506
S30 in S10	1732	575	1769	548	1840	518

Even though the EOFM supplies very precise strain maps, without a corresponding stress map, a good quantitative estimation of the Young's modulus of the inclusion is not possible (relative error of up to 144.1%). One issue of the presented conversion from strain to Young's modulus is that in some regions the strain is very small. Division by this small strain values leads to a high error in the Young's modulus, as indicated in Fig. 9. Another issue occurs when the inclusion is close to the upper or lower phantom boundary (e.g. smallS20inS10 or largeS20inS10, compare Fig. 12). At the upper and lower phantom boundaries, both OF and EOFM detect a high change in the gradient. The same is true for the inclusion boundary. If these regions overlap, the smoothness requirement inherent in OF and EOFM inhibits precise movement detection.

D. Intensity-Based Inversion Method (IIM)

To circumvent the missing stress map information, IIM can be used. The reconstructed Young's moduli of the background and inclusion for all samples using IIM are presented in Table III, and are depicted in Fig. 9 together with the ground truth values. The Young's modulus of the background material is found with high precision (relative error of 0.8-11.0%), and the generally more difficult inclusion stiffness can be computed precisely as well (relative error of 0.4-22.3%). The inclusions which are softer than their background were reconstructed more reliably than the stiffer inclusions. The background reconstruction works best for phantoms with a high background volume ratio.

The algorithm converges within 250 iterations for all samples, when the tolerance of 10^{-6} in the residual is reached.

Here, we summarize the advantages and limitations of IIM:

1) The IIM approach can be applied with any deformation model fitting to the experiment.
2) IIM depends on the OCT scan and segmentation quality.
3) The dimension reduction is advantageous for dealing with the ill-posedness of the inverse elasticity problem from one displacement measurement. Since it is not uncommon to perform an image segmentation of the scans in medical imaging, this additional information helps stabilizing the parameter reconstruction.
4) IIM can be performed for full inversion, i.e. without a piece-wise constant assumption made in Section II-J. However, the problem becomes computationally more demanding and requires a stronger stabilization.
5) The regularization parameter α has to be chosen small to avoid oversmoothing of the solutions.

In summary, we find that among all three considered reconstruction methods, IIM is most accurate and stable overall. The relative error of IIM to the ground truth is by a factor of 3.5 smaller than, the relative error of the EOFM based and the uniaxial method.

IV. CONCLUSION

In this paper, we presented an iterative inversion method for reconstructing the Young's modulus in OCT images and compared it to two strain-based reconstruction approaches.

For a comprehensive study of the considered methods, we analyzed a number of phantoms with different inclusion sizes and inclusion to background stiffness ratios. In all three methods, the reconstruction of the background worked best, being influenced only by the size of the inclusion. As expected, the higher the volume ratio of the background (the smaller the inclusion), the better the background reconstruction. The uniaxial reconstruction proved to be highly affected by lateral movement and therefore performed worst in our analysis. This underlines the importance of a multi-dimensional view on elastography.

We applied and evaluated the qualitative displacement and strain estimation method proposed in [43] and showed that even though the strain map can be precisely reconstructed, the corresponding stress information at each position is required in addition to estimate a valid Young's modulus stiffness map.

In quasi-static OCE, it is common to work under uniform stress assumptions, i.e., with only one axial stress value available for the whole sample. Gaining information about the distribution of stress inside a sample is a challenge. Using a compliance layer, one can obtain 2D *en face* stress information, but this still does not provide independent stress measurements for the individual A-scans, due to the smoothness of the deformation of this compliance layer. Accessing depth-resolved knowledge of the stress distribution is a difficult challenge for OCE. In our experiments, we observed that the Poisson's ratio corrects for neglecting the lateral direction in stress.

On the other hand, IIM is capable of reliably reconstructing the inclusion stiffness and achieves by far the best results. While the strain map based reconstruction can result in reduced precision, if the inclusion is close to the phantom border, IIM is insensitive to the location of the inclusion within the phantom. The application of IIM is not limited to two-area segmentations as done for the 12 samples considered in this work but can also be extended to a higher number of segments. Adaptation to any desired physical model is possible, e.g., to a viscoelastic or plastic sample description.

Currently, the proposed methods are dependent on optical contrast for deriving the segmentation, while OCE (especially phase-sensitive OCE) is known for being capable of visualizing stiff inclusions even without optical contrast [50]. In this paper, we showed that the lateral motion (which is not available in phase-sensitive OCE) is important for a valid reconstruction of the Young's modulus. In future work, a two step approach, combining both methods, could be used to achieve independence from optical contrast as well as a precise reconstruction performance. In a first step, phase-sensitive OCE could deliver a stiffness guess. This guess could serve as the basis for the segmentation and in a second step be refined using IIM.

Acknowledgment

The authors would like to thank Martin Stoiber for providing access to the TA Instruments tensile testing machine and Michael Niederleithner and Matthias Salas for their inital work on the OCT acquisition software.

Disclosures

The authors declare no conflicts of interest.

References

[1] I. Cespedes, J. Ophir, H. Ponnekanti, and N. Maklad, "Elastography: Elasticity imaging using ultrasound with application to muscle and breast in vivo," *Ultrason. Imag.*, vol. 15, no. 2, pp. 73–88, 1993.

[2] H.-J. Sommerfeld et al., "Prostatakarzinomdiagnostik durch ultraschallelastographie," *Der Urologe A*, vol. 42, no. 7, pp. 941–945, Jul. 2003. [Online]. Available: http://link.springer.com/10.1007/s00120-003-0297-4

[3] B. S. Garra et al., "Elastography of breast lesions: Initial clinical results.," *Radiology*, vol. 202, no. 1, pp. 79–86, Jan. 1997, doi: 10.1148/radiology.202.1.8988195.

[4] R. M. Sigrist, J. Liau, A. E. Kaffas, M. C. Chammas, and J. K. Willmann, "Ultrasound elastography: Review of techniques and clinical applications," *Theranostics*, vol. 7, no. 5, pp. 1303–1329, 2017. [Online]. Available: http://www.thno.org/v07p1303.htm

[5] S. J. Kim, H. J. Park, and S. Y. Lee, "Usefulness of strain elastography of the musculoskeletal system," *Ultrasonography*, vol. 35, no. 2, pp. 104–109, Apr. 2016, doi: 10.14366/usg.15072.

[6] R. Prado-Costa, J. Rebelo, J. Monteiro-Barroso, and A. S. Preto, "Ultrasound elastography: Compression elastography and shear-wave elastography in the assessment of tendon injury," *Insights Imag.*, vol. 9, no. 5, pp. 791–814, Oct. 2018. [Online]. Available: https://insightsimaging.springeropen.com/articles/10.1007/s13244-018-0642-1

[7] S. A. Kruse et al., "Tissue characterization using magnetic resonance elastography: Preliminary results*," *Phys. Med. Biol.*, vol. 45, no. 6, pp. 1579–1590, Jun. 2000. [Online]. Available: http://stacks.iop.org/0031-9155/45/i=6/a=313?key=crossref.93cb122fa9e01fcec20d215baf5dc6b8

[8] P. Kennedy et al., "Magnetic resonance elastography vs. point shear wave ultrasound elastography for the assessment of renal allograft dysfunction," *Eur. J. Radiol.*, vol. 126, May 2020, Art. no. 108949. [Online]. Available: https://linkinghub.elsevier.com/retrieve/pii/S0720048X20301388

[9] G. Low, "General review of magnetic resonance elastography," *World J. Radiol.*, vol. 8, no. 1, pp. 59–72, 2016. [Online]. Available: http://www.wjgnet.com/1949-8470/full/v8/i1/59.htm

[10] A. Kolipaka, R. D. White, and R. L. Ehman, "Chapter 21 - Magnetic resonance elastography for arterial wall characterization," in *Biomechanics of Coronary Atherosclerotic Plaque* (Biomechanics of Living Organs Series), vol. 4, J. G. Ohayon Finet and R. I. Pettigrew, Eds. San Diego, CA, USA: Academic Press, 2020, pp. 491–515. [Online]. Available: http://www.sciencedirect.com/science/article/pii/B9780128171950000214

[11] R. Sinkus et al., "High-resolution tensor MR elastography for breast tumour detection," *Phys. Med. Biol.*, vol. 45, no. 6, pp. 1649–1664, Jun. 2000. [Online]. Available: http://stacks.iop.org/0031-9155/45/i=6/a=317?key=crossref.9daa10efcf53d8425c8b0eb31857764b

[12] R. Highnam, J. Brady, and B. Shepstone, "Mammographic image analysis," *Eur. J. Radiol.*, vol. 24, no. 1, pp. 20–32, Jan. 1997. [Online]. Available: https://linkinghub.elsevier.com/retrieve/pii/S0720048X96011102

[13] N. Karssemeijer, "Adaptive noise equalization and recognition of microcalcificatio clusters in mammograms," *Int. J. Pattern Recognit. Artif. Intell.*, vol. 07, no. 06, pp. 1357–1376, Dec. 1993. [Online]. Available: https://www.worldscientific.com/doi/abs/10.1142/S0218001493000662

[14] T. B. Edrington, K. Zadnik, and J. T. Barr, "Keratoconus," *Optometry Clin.: Official Pub. Prentice Soc.*, vol. 4, no. 3, pp. 65–73, 1995.

[15] M. J. A. Girard et al., "Translating ocular biomechanics into clinical practice: Current state and future prospects," *Curr. Eye Res.*, vol. 40, no. 1, pp. 1–18, Jan. 2015. [Online]. Available: http://www.tandfonline.com/doi/full/10.3109/02713683.2014.914543

[16] P. Segers, E. R. Rietzschel, and J. A. Chirinos, "Brief review on how to measure arterial stiffness in humans," *Arteriosclerosis, Thrombosis, Vasc. Biol.*, vol. 40, pp. 1034–1043, Dec. 2019. [Online]. Available: https://www.ahajournals.org/doi/10.1161/ATVBAHA.119.313132

[17] D. Huang et al., "Optical coherence tomography," *Science*, vol. 254, no. 5035, pp. 1178–1181, 1991. [Online]. Available: https://science.sciencemag.org/content/254/5035/1178

[18] J. M. Schmitt, "OCT elastography: Imaging microscopic deformation and strain of tissue," *Opt. Exp.*, vol. 3, no. 6, pp. 199–218, Sep. 1998 . [Online]. Available: https://www.osapublishing.org/abstract.cfm?URI=oe-3-6-199

[19] S. J. Kirkpatrick, R. K. Wang, and D. D. Duncan, "OCT-based elastography for large and small deformations," *Opt. Exp.*, vol. 14, no. 24, Nov. 2006, Art. no. 11585. [Online]. Available: https://www.osapublishing.org/abstract.cfm?URI=oe-14-24-11585

[20] A. Nair, M. Singh, S. Aglyamov, and K. V. Larin, "Heartbeat optical coherence elastography: Corneal biomechanics in vivo," *J. Biomed. Opt.*, vol. 26, no. 02, Feb. 2021, Art. no. 020502. [Online]. Available: https://www.spiedigitallibrary.org/journals/journal-of-biomedical-optics/volume-26/issue-02/020502/Heartbeat-optical-coherence-elastography-corneal-biomechanics-in-vivo/10.1117/1.JBO.26.2.020502.full

[21] B. F. Kennedy et al., "Strain estimation in phase-sensitive optical coherence elastography," *Biomed. Opt. Exp.*, vol. 3, no. 8, pp. 1865–1879, Aug. 2012. [Online]. Available: https://www.osapublishing.org/boe/abstract.cfm?uri=boe-3-8-1865

[22] J. Zhu et al., "3D mapping of elastic modulus using shear wave optical micro-elastography," *Sci. Rep.*, vol. 6, no. 1, Dec. 2016, Art. no. 35499. [Online]. Available: http://www.nature.com/articles/srep35499

[23] L. Mullins, "Softening of rubber by deformation," *Rubber Chem. Technol.*, vol. 42, no. 1, pp. 339–362, Mar. 1969, doi: 10.5254/1.3539210.
[24] X. Liang, A. L. Oldenburg, V. Crecea, E. J. Chaney, and S. A. Boppart, "Optical micro-scale mapping of dynamic biomechanical tissue properties," *Opt. Exp.*, vol. 16, no. 15, Jul. 2008, Art. no. 11052. [Online]. Available: https://www.osapublishing.org/oe/abstract.cfm?uri=oe-16-15-11052
[25] F. Zvietcovich and K. V. Larin, "Wave-based optical coherence elastography: The 10-year perspective," *Prog. Biomed. Eng.*, vol. 4, no. 1, Jan. 2022, Art. no. 012007. [Online]. Available: https://iopscience.iop.org/article/10.1088/2516-1091/ac4512
[26] V. Y. Zaitsev et al., "Strain and elasticity imaging in compression optical coherence elastography: The two decade perspective and recent advances," *J. Biophotonics*, vol. 14, no. 2, Feb. 2021, Art. no. e202000257. [Online]. Available: https://onlinelibrary.wiley.com/doi/10.1002/jbio.202000257
[27] M. M. Doyley, "Model-based elastography: A survey of approaches to the inverse elasticity problem," *Phys. Med. Biol.*, vol. 57, no. 3, pp. R35–R73, Feb. 2012. [Online]. Available: https://iopscience.iop.org/article/10.1088/0031-9155/57/3/R35
[28] J. Li, M. S. Hepburn, L. Chin, A. Mowla, and B. F. Kennedy, "Analysis of sensitivity in quantitative micro-elastography," *Biomed. Opt. Exp.*, vol. 12, no. 3, Mar. 2021, Art. no. 1725. [Online]. Available: https://opg.optica.org/abstract.cfm?URI=boe-12-3-1725
[29] P. Wijesinghe, L. Chin, and B. F. Kennedy, "Strain tensor imaging in compression optical coherence elastography," *IEEE J. Sel. Topics Quantum Electron.*, vol. 25, no. 1, pp. 1–12, Jan./Feb. 2019. [Online]. Available: https://ieeexplore.ieee.org/document/8470111/
[30] K. Kurokawa, S. Makita, Y.-J. Hong, and Y. Yasuno, "In-plane and out-of-plane tissue micro-displacement measurement by correlation coefficients of optical coherence tomography," *Opt. Lett.*, vol. 40, no. 9, May 2015, Art. no. 2153. [Online]. Available: https://opg.optica.org/abstract.cfm?URI=ol-40-9-2153
[31] V. Y. Zaitsev et al., "Deformation-induced speckle-pattern evolution and feasibility of correlational speckle tracking in optical coherence elastography," *J. Biomed. Opt.*, vol. 20, no. 7, Jul. 2015, Art. no. 075006, doi: 10.1117/1.JBO.20.7.075006.
[32] C. Sun, B. Standish, B. Vuong, X.-Y. Wen, and V. Yang, "Digital image correlation–based optical coherence elastography," *J. Biomed. Opt.*, vol. 18, no. 12, Dec. 2013, Art. no. 121515, doi: 10.1117/1.JBO.18.12.121515.
[33] D. D. Duncan and S. J. Kirkpatrick, "Processing algorithms for tracking speckle shifts in optical elastography of biological tissues," *J. Biomed. Opt.*, vol. 6, no. 4, 2001, Art. no. 418, doi: 10.1117/1.1412224.
[34] X. Liu, F. Zaki, H. Garg, and J. Rodriguez, "OCE quantification of Poisson's ratio through 2D speckle tracking," *Proc. SPIE*, vol. 10880, 2019, pp. 74–77. [Online]. Available: https://www.spiedigitallibrary.org/conference-proceedings-of-spie/10880/2503856/OCE-quantification-of-Poissons-ratio-through-2D-speckle-tracking/10.1117/12.2503856.full
[35] A. Nahas, M. Bauer, S. Roux, and A. C. Boccara, "3D static elastography at the micrometer scale using full field OCT," *Biomed. Opt. Exp.*, vol. 4, no. 10, Oct. 2013, Art. no. 2138. [Online]. Available: https://opg.optica.org/boe/abstract.cfm?uri=boe-4-10-2138
[36] S. Wei and J. U. Kang, "Optical flow optical coherence tomography for determining accurate velocity fields," *Opt. Exp.*, vol. 28, no. 17, Aug. 2020, Art. no. 25502. [Online]. Available: https://opg.optica.org/abstract.cfm?URI=oe-28-17-25502
[37] S. Kling, E. A. Torres-Netto, B. Spiru, W. Sekundo, and F. Hafezi, "Quasi-static optical coherence elastography to characterize human corneal biomechanical properties," *Invest. Opthalmol. Vis. Sci.*, vol. 61, no. 6, pp. 29–37, Jun. 2020. [Online]. Available: https://iovs.arvojournals.org/article.aspx?articleid=2770134
[38] S. K. Han et al., "Optical coherence tomographic elastography reveals mesoscale shear strain inhomogeneities in the annulus fibrosus," *Spine*, vol. 41, no. 13, pp. E770–E777, Jul. 2016. [Online]. Available: https://journals.lww.com/00007632-201607010-00006
[39] B. Horn and B. Schunck, "Determining optical flow," *Artif. Intell.*, no. 17, pp. 185–203, 1981. [Online]. Available: http://hdl.handle.net/1721.1/6337
[40] Y. Okafuji and T. Fukao, "Theoretical interpretation of drivers' gaze strategy influenced by optical flow," *Sci. Rep.*, vol. 11, no. 1, Dec. 2021, Art. no. 2389. [Online]. Available: http://www.nature.com/articles/s41598-021-82062-1
[41] J. Scholler et al., "Probing dynamic processes in the eye at multiple spatial and temporal scales with multimodal full field OCT," *Biomed. Opt. Exp.*, vol. 10, no. 2, pp. 731–746, Feb. 2019. [Online]. Available: http://opg.optica.org/boe/abstract.cfm?URI=boe-10-2-731
[42] E. Sherina, L. Krainz, S. Hubmer, W. Drexler, and O. Scherzer, "Displacement field estimation from OCT images utilizing speckle information with applications in quantitative elastography," *Inverse Problems*, vol. 36, no. 12, 2020, Art. no. 124003.
[43] E. Sherina, L. Krainz, S. Hubmer, W. Drexler, and O. Scherzer, "Challenges for optical flow estimates in elastography," in *Proc. 8th Int. Conf. Scale Space Variational Methods Comput. Vis.*, A. Elmoataz, J. Fadili, Y. Queau, J. Rabin, and L. Simon, Eds., Berlin, Germany: Springer, 2021, pp. 128–139.
[44] Q. Fang et al., "Handheld probe for quantitative micro-elastography," *Biomed. Opt. Exp.*, vol. 10, no. 8, Aug. 2019, Art. no. 4034. [Online]. Available: https://www.osapublishing.org/abstract.cfm?URI=boe-10-8-4034
[45] Y. Qiu, F. R. Zaki, N. Chandra, S. A. Chester, and X. Liu, "Nonlinear characterization of elasticity using quantitative optical coherence elastography," *Biomed. Opt. Exp.*, vol. 7, no. 11, Nov. 2016, Art. no. 4702. [Online]. Available: https://www.osapublishing.org/abstract.cfm?URI=boe-7-11-4702
[46] R. W. Sanderson, A. Curatolo, P. Wijesinghe, L. Chin, and B. F. Kennedy, "Finger-mounted quantitative micro-elastography," *Biomed. Opt. Exp.*, vol. 10, no. 4, Apr. 2019, Art. no. 1760. [Online]. Available: https://www.osapublishing.org/abstract.cfm?URI=boe-10-4-1760
[47] G. Lamouche et al., "Review of tissue simulating phantoms with controllable optical, mechanical and structural properties for use in optical coherence tomography," *Biomed. Opt. Exp.*, vol. 3, no. 6, Jun. 2012, Art. no. 1381. [Online]. Available: https://www.osapublishing.org/boe/abstract.cfm?uri=boe-3-6-1381
[48] C. Schnörr, "Determining optical flow for irregular domains by minimizing quadratic functionals of a certain class," *Int. J. Comput. Vis.*, vol. 6, no. 2, pp. 25–37, 1991.
[49] J. A. Nelder and R. Mead, "A simplex method for function minimization," *Comput. J.*, vol. 7, no. 4, pp. 308–313, 1965, doi: 10.1093/comjnl/7.4.308.
[50] K. M. Kennedy, C. Ford, B. F. Kennedy, M. B. Bush, and D. D. Sampson, "Analysis of mechanical contrast in optical coherence elastography," *J. Biomed. Opt.*, vol. 18, no. 12, Nov. 2013, Art. no. 121508, doi: 10.1117/1.JBO.18.12.121508.

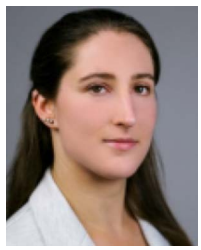

Lisa Krainz (Graduate Student Member, IEEE) received the M.Sc. degree in biomedical engineering from the Technical University of Vienna, Vienna, Austria. She is currently working toward the Ph.D. degree with the Center of Medical Physics and Biomedical Engineering, Medical University of Vienna, Vienna, where she investigates photoacoustic tomography and optical coherence tomography as tools for microscale elastography. She worked in the fields of biosensors and quantum cryptography with AIT, Seibersdorf, Austria.

Ekaterina Sherina received the Diploma in mathematics from the Tomsk State University, Tomsk, Russia, in 2010, and the Ph.D. degree in mathematics from the Technical University of Denmark, Kongens Lyngby, Denmark, in 2018. She is currently a Postdoctoral Researcher with the Faculty of Mathematics, University of Vienna, Vienna, Austria. Her research interests include inverse problems, regularization and image processing, especially on iterative inversion methods for parameter and motion reconstruction problems, and processing methods with application to OCT data.

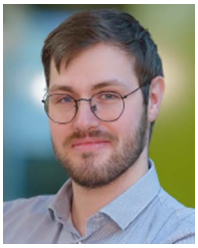

Simon Hubmer received the Doctorate degree in mathematics from Johannes Kepler University, Linz, Austria. He is currently a Postdoctoral Researcher with the Johann Radon Institute, Linz. His research interests include the design, analysis, and application of efficient regularization methods for the solution of inverse problems, in particular for tomographic imaging problems across the scales.

Mengyang Liu received the bachelor's degree from the Harbin Institute of Technology, Harbin, China, in 2008, the master's degree from the University of Delaware, Newark, DE, USA, in 2011, and the Ph.D. degree from the Medical University of Vienna, Vienna, Austria, in 2015. As a Marie Skłodowska-Curie Global Fellowship holder, he has a dual appointment in 2022 with the Singapore Eye Research Institute, Singapore, as a Research Fellow and with the Medical University of Vienna, as an EU Visiting Scholar. His research focuses on multimodal optical imaging.

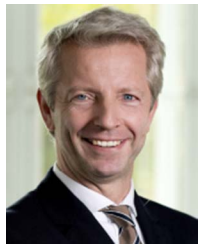

Wolfgang Drexler is currently a Full Professor and the Head of the Center for Medical Physics and Biomedical Engineering, Medical University of Vienna, Vienna, Austria. From 2006 to 2009, he was a Full Professor of biomedical imaging with Cardiff University, Cardiff, Wales, U.K. From 1998 to 1999, he was with MIT, Cambridge, MA, USA.He was the recipient of the Austrian START Award (2001) and the COGAN Award (2007). His H-index is 75 (Scopus), and thje Research Grant Income since 2000 is €17 million.

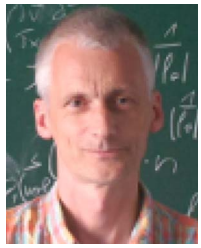

Otmar Scherzer is currently a Full Professor with the Faculty of Mathematics, University of Vienna, Vienna, Austria. He is also the Head of the Special Research Program Tomography Across the Scales and the Christian-Doppler Laboratory for modelling and simulation of novel ultrasound devices. His research interests in which he made substantial contributions include the fields of regularization theory and inverse problems, coupled physics imaging, optics, and ultrasound imaging. He was the recipient of the EAIP Award for outstanding scientific contributions to the field of inverse problems.